1D MoO₃ Nanorods Decorated by Palladium Nanoparticles: Surface Plasmon Resonance Promoted Photodegradation of Congo Red Dye

L.T. Parvathi[1,2] and S. Karuthapandian[1,*]

[1]Department of Chemistry, V.H.N. Senthikumara Nadar College (Autonomous), Virudhunagar-626001, India
[2]Department of Chemistry, Sri Kaliswari College (Autonomous), Sivakasi-626123, India

*Corresponding author: E-mail: drpandianskvhnsnc2007@gmail.com

In this work, 1D, MoO₃ palm leaf shaped nanorods decorated by palladium nanoparticle for the photodegradation of organic pollutant. The Pd loaded MoO₃ ratio were optimized and 2% Pd loaded MoO₃ shows excellent photodegradation towards the organic pollutants. The synthesized Pd decorated MoO₃ nanorods were characterized by various analytical tools such as TEM, SEM, BET, EDX, XRD, UV-DRS *etc*., The TEM and SEM results revealed that the palm leaf shaped MoO₃ nanorods was well decorated by Pd metals. The crystallite size of MoO₃ was decreased when increases the palladium loading percentage. The surface area of MoO₃ lowered when palladium loaded. The prepared nanocomposites were in high purity confirmed by EDX analysis. The energy gap tailored into visible region by loaded palladium. The catalytic efficiency of the prepared nanocomposites were tested against the photo degradation of organic pollutant within 60 min and rate constant also calculated. The catalyst was not much lower their activity even five reusability. The OH⁻ and h⁺ (holes) were the active species involved in the photodegradation mechanism.

Keywords: Pd@MoO₃, Surface plasmon, Photocatalyst, Photodegradation, Visible light.

INTRODUCTION

Wastewater effluents discharged from textile industries is a severe threat not only on human life but also on the environment and hence demand suitable remediation technology [1-3]. Especially organic dyes are the compounds that are more stable and most easily recognizable in water system and hence create life threatening situation [4,5]. In this regards, various techniques such as adsorption, membrane filtration, chemical oxidation, biological digestion, electrochemical and advanced oxidation process (AOPs) broadly recognized for the abatement of organic pollutant from water [6-8]. Among these methods, AOPs based semiconductor photocatalytic degradation process has proved to be an efficient and eco-friendly technique compared to the other techniques.

Molybdenum trioxide (MoO₃) is a most noticeable star nanomaterial for environmental treatment due to their structural stability and unique electronic surface properties [9]. MoO₃ is a wide band gap n-type transition metal oxide semiconductor whose conductivity is due to vacant oxygen orbitals [10-12].

In addition, MoO₃ is a polymorph material with at least four crystalline phases such as thermodynamically stable orthorhombic (α-MoO₃), hexagonal (*h*-MoO₃), metastable monoclinic (β-MoO₃) and high pressure monoclinic (MoO₃-II) [13,14]. Compared to other phases, α-MoO₃ is one of the unique materials because of its excellent electrochemical performance and photocatalytic activities as well as the promising stability [15-17]. However, low quantum yield and higher recombination rate of photogenerated charge carriers (electron-hole pairs), which hampered the wastewater remediation application of MoO₃ in photocatalyst. To solve this problem, several strategies are including heterostructure formation with other semiconductor, metal or non-metal doping and surface modification have been conducted to design or develop new MoO₃ photocatalytic material.

Lately, doping of noble metals (Ag, Au, Pd and Pt) with semiconductor has been receiving considerable attention because it is easy, convenient and effective method for the delay/prevent the recombination and enhancing the stability of MoO₃ [18]. Among them, palladium is one of the promising metals, which

has a beneficial influence on the photocatalytic activity of MoO_3 nanomaterial by effective transfer and inhibiting the photo-induced charge carriers recombination process. Moreover, palladium nanoparticles exhibit the surface plasmon resonance (SPR) effect has been recognized to provide a new way of enhancing the photocatalytic activity of MoO_3 [19,20]. Therefore, in this work, a series of palladium nanoparticles decorated 1D-MoO_3 nanorods were constructed by facile and inexpensive hydrothermal methods. The crystal structure, morphology, elemental compositions and optical properties of palladium loaded MoO_3 nanocomposites were systematically analyzed by various characterizations tools. The photocatalytic performance of pure MoO_3 and palladium loaded MoO_3 nanocomposites with different palladium loading level under visible light was evaluated by using Congo red as the model pollutant for degradations [21]. Finally, the possible mechanism for the photocatalytic degradation process was discussed and proposed.

EXPERIMENTAL

All reagents and chemicals employed for the synthesis and reaction process (Analytical grade) are used without further purification process. Ammonium heptamolybdate tetrahydrate $((NH_4)_6Mo_7O_{24}\cdot4H_2O)$, $NaBH_4$, palladium acetate, Congo red dye and ethanol were purchased from Sigma-Aldrich Chemicals. Deionized water was used for the preparation of all solutions.

Preparation Pd@MoO₃ nanorods: MoO_3 nanorods were synthesized by simple one-pot hydrothermal method. In a typical procedure, certain amount of ammonium heptamolybdate tetrahydrate was dissolved into 45 mL distilled water under constant stirring condition. Then, 5 mL of HCl was added drop wise and the mixture of solution was stirred another 1 h at room temperature. After 1 h, the mixture was transferred into a 100 mL Teflon-lined autoclave. The hydrothermal reaction was taken place at 160 ºC for 12 h. The resulted precipitate was filtered, washed with distilled water and dried in an oven at 80 ºC and to eliminate the volatile foreign matter. The Pd doped MoO_3 nanocomposites were prepared *via* usual ultrasonic method. The synthesized MoO_3 nanorods were added in a 50 mL of water for 30 min under ultrasound sonication. Next, the calculated amount of palladium acetate was inserted into the above solution. Finally, 1 M of 5 mL of $NaBH_4$ solution was added into the mixture of solution and then solution holding for another 30 min with ultrasound sonication. Palladium nanoparticles were obtained by reducing of palladium acetate and then products were washed with water for several times and dried at 80 ºC for 12 h.

Analysis of samples: The synthesized pure MoO_3 nanorods and Pd doped MoO_3 nanocomposites were investigated by various analytical tools to characterize their morphological, crystal structure, optical and photocatalytic properties. The morphologies of as-synthesized nanomaterials were examined by scanning electron microscopy (SEM-VEGA3 TESCAN) and transmission electron microscopy (TEM-PHILIPS CM 200 model). The structural crystallinity, crystal phases and crystalline sizes were investigated by X-ray diffraction (PANalytical-Xpert Pro.) pattern measured with CuKα radiation ($\lambda = 1.54178$ Å) in the range of 10-80º. To study the elemental compositions

of as prepared catalysts were examined by energy dispersive spectroscopy (BRUKER-Nano GmbH, X-50 flash Detector) attached with SEM. Specific surface area and pore sizes were restrained with liquid N_2 using a (Micromeritics ASAP-2020) porosimeter instrument by the Brunauer-Emmett-Teller (BET). Pore size distribution plots were draw from Barret-Joyner-Halenda (BJH) method. The absorption spectral data was used to determine the type of optical band gap present in the samples (UV-DRS-2400 in the range of 200-800 nm, Shimadzu).

Photocatalytic activity: The photocatalytic activity of as-synthesized pure MoO_3 and a series of Pd doped MoO_3 nanocomposites were evaluated by photodegradation of Congo red dye solution at ambient temperature. In a typical procedure, 50 mg of catalyst was immersed into 100 mL of dye pollutant (10 mg/L) under magnetically stirring for 30 min in the dark to achieve the adsorption-desorption equilibrium. 150 W Xe light was used as the visible-light sources at 15 cm away from the solution. During the experiments, 5 mL aliquot was collected in a certain time interval. Followed by, the concentration of dye pollutant solution was detected on a UV-Vis spectrophotometer (UV-2600, Shimadzu, Japan). To evaluate the stability and reusability of catalyst, the nanocomposites were collected by centrifuged at 8500 rpm for 10 min from the suspension, and then the recovered photocatalyst was used for subsequent cycle test.

$$\text{Photodegradation efficiency (\%)} = \left(1 - \frac{C}{C_o}\right) \times 100$$
$$= \left(1 - \frac{A}{A_o}\right) \times 100 \quad (1)$$

where A_o and C_o are the initial absorbance of Congo red dye solution at 498 nm and initial concentration, while A and C are the absorbance of Congo red dye solution at 498 nm and the concentration after visible light irradiation at any time.

RESULTS AND DISCUSSION

XRD analysis: The phase purity and crystallinity were investigated by X-ray diffraction (XRD) analysis. The five intense Bragg diffraction peaks at 2θ = 12.7º (020), 23.4º (110), 25.7º (040), 27.2º (021) and 38.9º (060), which are the characteristic of orthorhombic phase α-MoO_3 with high crystalline nature. The as-prepared MoO_3 material exhibits a set of well-defined reflex ions that were readily indexed as pure ortho-rhombic MoO_3 phase with standard JCPDS card no. 35-0609 and no characteristic peaks of impurities such as PdO were observed (Fig. 1). The XRD pattern belongs to orthorhombic α-MoO_3 phase with cell parameters are $a = 3.963$, $b = 13.85$ and $c = 3.696$ Å. The diffraction peaks intensity also decreases with Pd loading which arises from lattice distortion induced by Pd nanoparticles. The positions of Bragg diffraction peaks of Pd doped MoO_3 over the 2θ of 22-29º seem to shift to lower angle side and broadening of peaks which was due to the partial replacement or disorder of lattice (increase in lattice spacing) of Pd loaded on the crystal lattice of MoO_3. The shift of peaks position indicates that Pd nanoparticles have been successfully
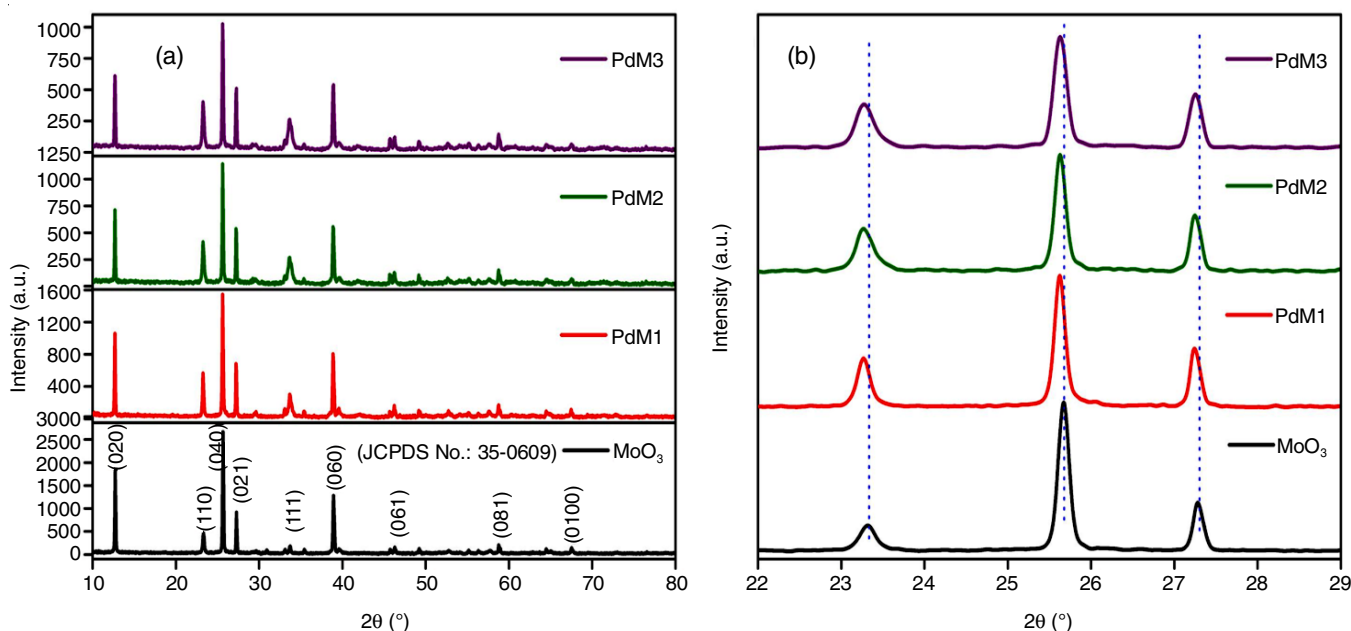
Fig. 1. XRD patterns of pure α-MoO₃ and Pd loaded α-MoO₃ nano-composite with different Pd loading concentration (1, 2 and 3%) (a) and an enlarged view 22-29° (b)

doped into the MoO₃ crystal lattice. Therefore, in XRD analysis implies the successful formation of Pd doped MoO₃ nanocomposites and no impurity phases were detected.

The average crystalline size of α-MoO₃ and Pd doped MoO₃ nanocomposites were determined by the full width at half maximum (FWHM) of the X-ray diffraction peak using Scherrer's equation [22] as follows:

$$D = \frac{k\lambda}{\beta\cos\theta} \qquad (2)$$

where D is the crystallite size, λ is wavelength of X-ray (λ = 0.154 nm), β is (full width at half maximum) FWHM of the diffraction peak, θ is glancing angle and k is Scherrer's constant. The crystallite sizes were calculated using reflection of plane (040) and the corresponding crystallite size of α-MoO₃ was 47 nm and Pd doped MoO₃ nanocomposites (1, 2 and 3%) were 41, 36 and 30 nm, respectively. The above results shows that Pd loading percentage increases the crystallite size was gradually decreases which means the Pd well in bounded on MoO₃ matrix.

Morphological analysis: The morphological and micro structures evolution was investigated by field-emission scanning electron microscopy (FESEM). The FESEM micro images of α-MoO₃ and Pd@MoO₃ nanocomposite as shown in Fig. 2. The FESEM images of Fig. 2a-b confirm that α-MoO₃ exhibits nanorods palm leaf shaped morphological structures. The surface of α-MoO₃ nanorods is very smooth and clean and the large number perfect 1D nanorods were combined with one another. After the incorporation of Pd, the Pd nanoparticles were evenly distributed on the surface of α-MoO₃ nanorods, which is clearly displayed in Fig. 2c-d.

The surface morphology and size of α-MoO₃ and Pd@MoO₃ particles were further evidenced using transmission electron microscopy (TEM). Fig. 3a-b display TEM images of α-MoO₃,

from which the 1D MoO₃ palm leaf shaped nanorod morphology can be clearly identified and the corresponding selected area diffraction (SAED) pattern (Fig. 3c) indicates that MoO₃ nano-plates grew along the (021) plane, which is in line with the XRD results. The interplanar spacing along the direction is determined to be 0.368 nm. The value is corresponding to d_{021} of orthorhombic XRD.

Fig. 3d-e exhibited the TEM images of Pd@MoO₃. Fig. 3f corresponds to the SAED pattern of Pd doped nanocomposite. The TEM image evidences that two distinct clear lattice fringers, which showed d = 0.303 and d = 0.24 nm corresponding to the (110) assigned to the orthorhombic phase of MoO₃ and (111) planes of palladium. No agglomeration of palladium on MoO₃ was observed.

As can be seen in the energy dispersive X-ray spectrometer (EDX) spectrum of the pure α-MoO₃ and 2% Pd doped MoO₃ nanocomposite were displayed in Fig. 4a-b, respectively. Fig. 4a shows α-MoO₃ consist of two elements *i.e.* Mo and O without any other impurity element peaks and the molar ratio of Mo:O measured by the EDX was nearly 3:1, corresponding to the chemical formula of α-MoO₃ phase. The EDX spectrum (Fig. 4b) reveals that 2% of Pd doped MoO₃ nanocomposite consists of three elements only (Mo, Pd and O).

Surface area analysis: The surface area and porous structure of pure α-MoO₃, 2% Pd doped MoO₃ nanoocompo-site were inferred from their nitrogen adsorption-desorption isotherms (Fig. 5). The Brunauer-Emmett-Teller (BET) specific surface area for MoO₃ and 2% Pd doped MoO₃ were 6.98 and 4.61 m² g⁻¹, respectively. Compared to pure MoO₃, 2% Pd doped MoO₃ nanocomposite shows the lower surface area, which might be due to the pore blockage effect between Pd nanoparticles and MoO₃. Furthermore, the inset figure shows the pore-size distributions plot was acquired using Barrett-Joyner-Halenda (BJH) method from the desorption isotherm. The average pore
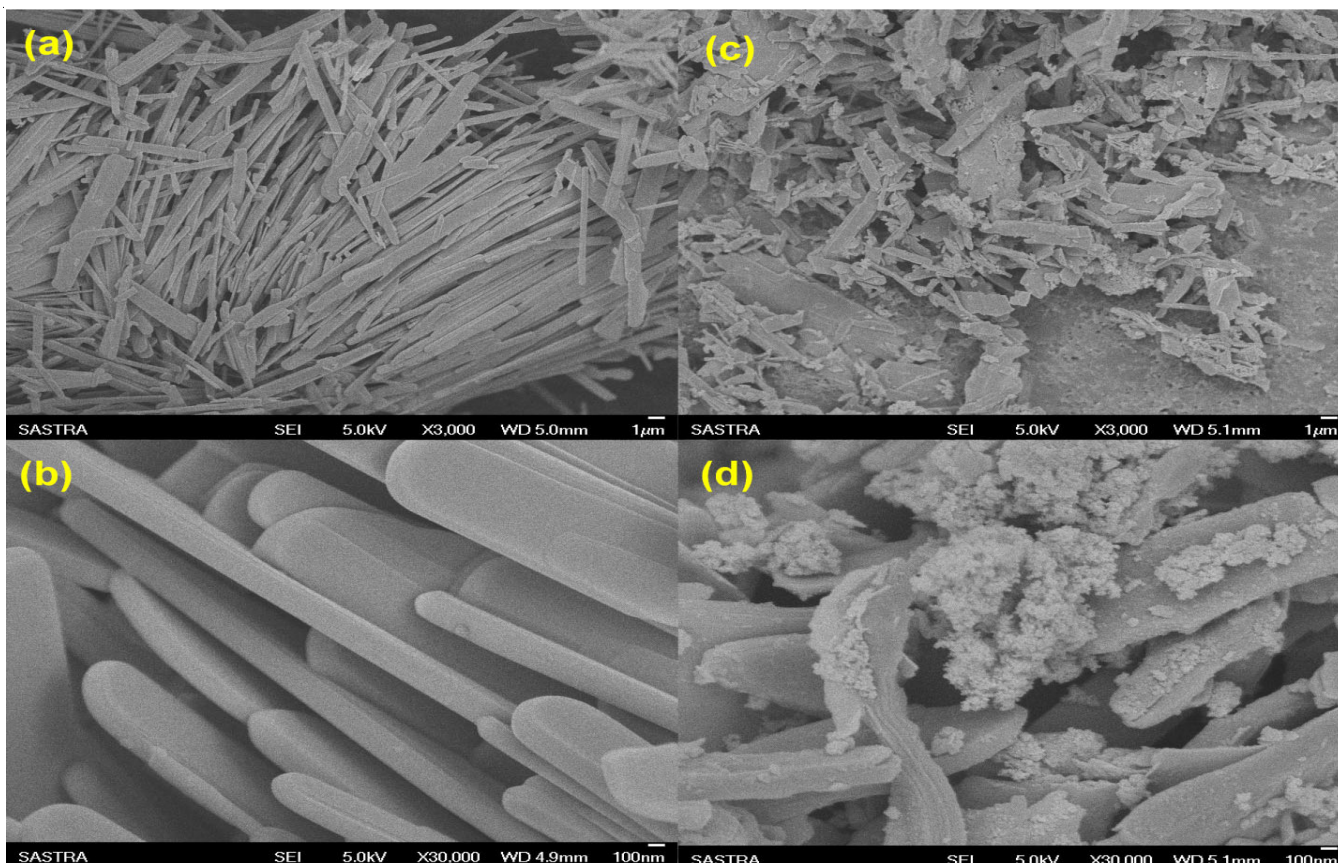
Fig. 2. SEM micro images of (a, b) pristine α-MoO₃ and (c, d) (2%) Pd loaded α-MoO₃ nanocomposite
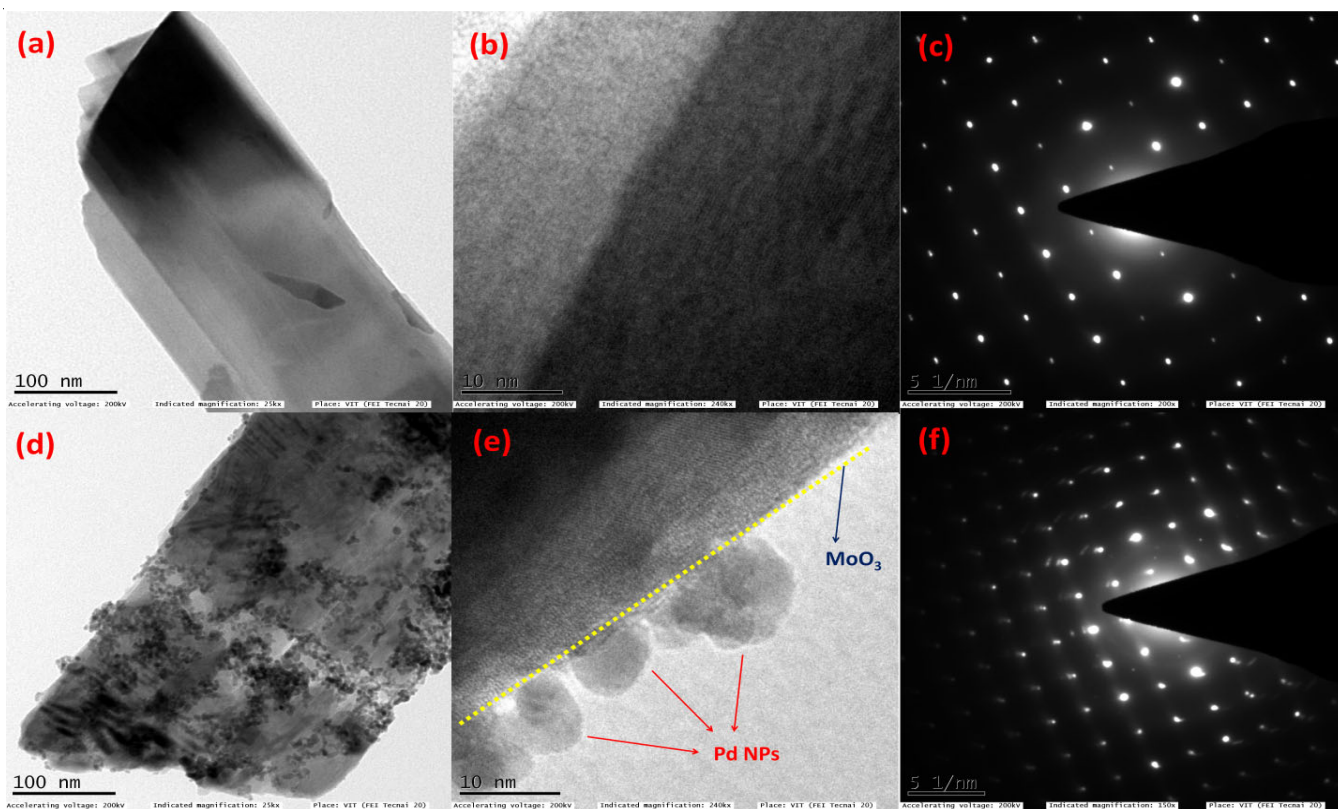
Fig. 3. TEM micro images of (a, b) pristine α-MoO₃, TEM micro images of (c) α-MoO₃ (SAED) pattern and (d,e) (2%) Pd loaded α-MoO₃ nanocomposite, TEM micro images of (f) (2%) Pd loaded α-MoO₃ (SAED) pattern
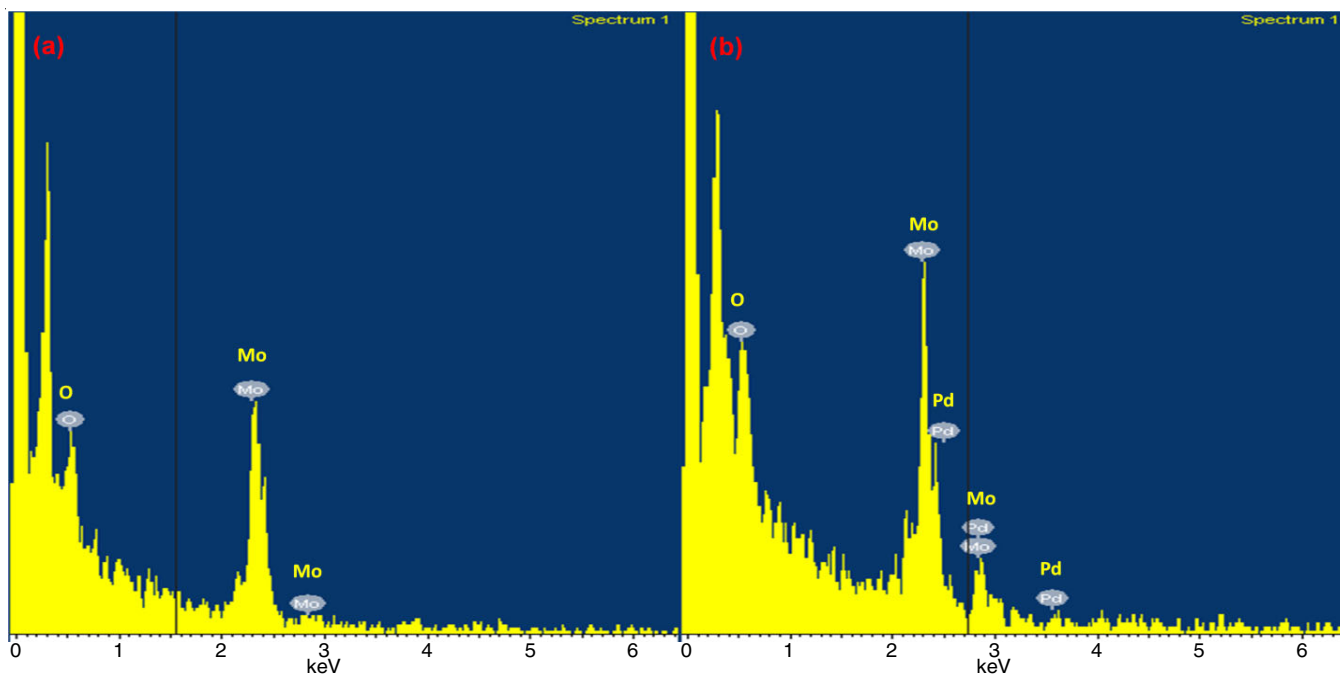
Fig. 4. EDX spectra and elemental mapping of pristine α-MoO₃ (a) and (2%) Pd loaded α-MoO₃ nanocomposite (b)
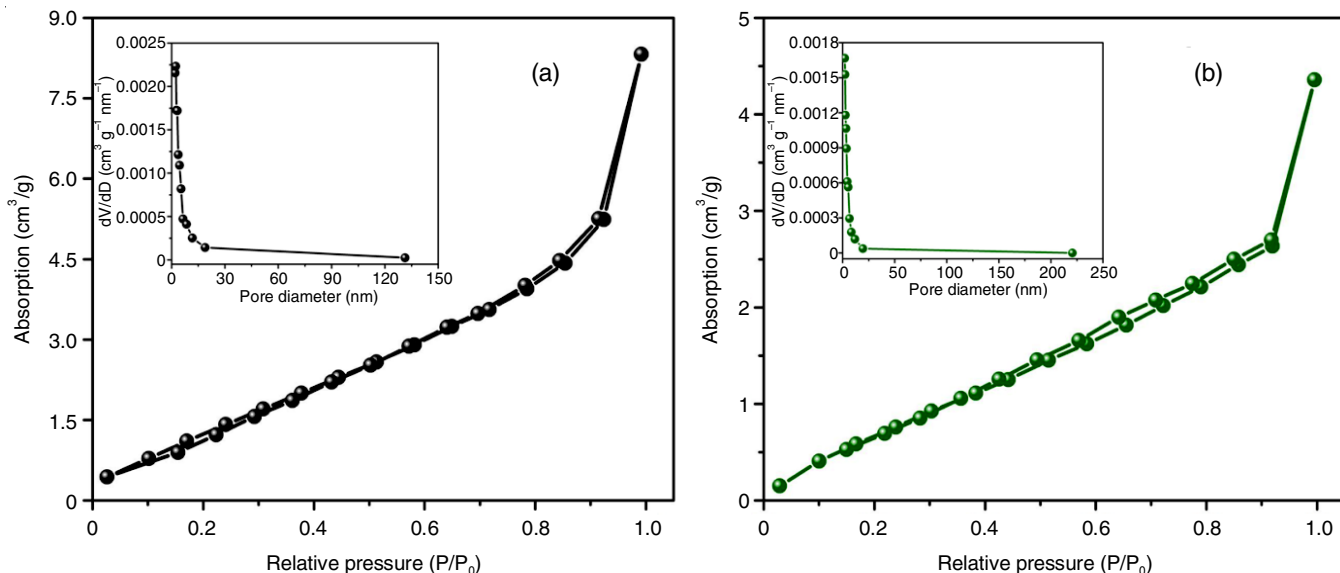
Fig. 5. Nitrogen adsorption-desorption curves of pristine α-MoO₃ (a) and (2%) Pd loaded α-MoO₃ nanocomposite (b). Inset shows the BJH pore size distribution curves

volumes of MoO₃ and 2% Pd doped MoO₃ nanocomposite was 0.018 and 0.011 cm³/g, respectively. These results indicates that more aggregate nanoparticles leads to the less pore volume hence reduced surface area of nanomaterials.

Optical properties: The energy band gap and optical properties of pure α-MoO₃, Pd doped MoO₃ samples were studied by UV-vis diffuse reflectances pectra (UV-visible DRS) are shown in Fig. 6. The strong light absorption in the visible light region from 350 to 450 nm for pristine α-MoO₃, which may be due to the effective band gap transitions of α-MoO₃ (conduction band molybdenum 4d shell to valence band oxygen 2p shell) [23,24]. After loading of palladium, an absorption intensity in the visible region apparently increased which probably

because of the surface plasmon resonance (SPR) effect of Pd nanoparticles. From these observations, Pd nanoparticles can be generating more number of hot electrons and holes and enhance the utilization efficiency of solar light by adsorbing huge amount of visible light photons [25,26]. It is amazing to note that clear broad absorption band was observed in the range of 500-600 nm in the Pd doped MoO₃ nanocomposites. This result suggests that it (α-MoO₃, Pd doped MoO₃) may be used as a hopeful candidate for visible absorbing semiconductor materials and used for the organic pollutant degradations.

$$(\alpha) = \frac{A}{h\nu(h\nu - E_g)^{-1/2}}$$
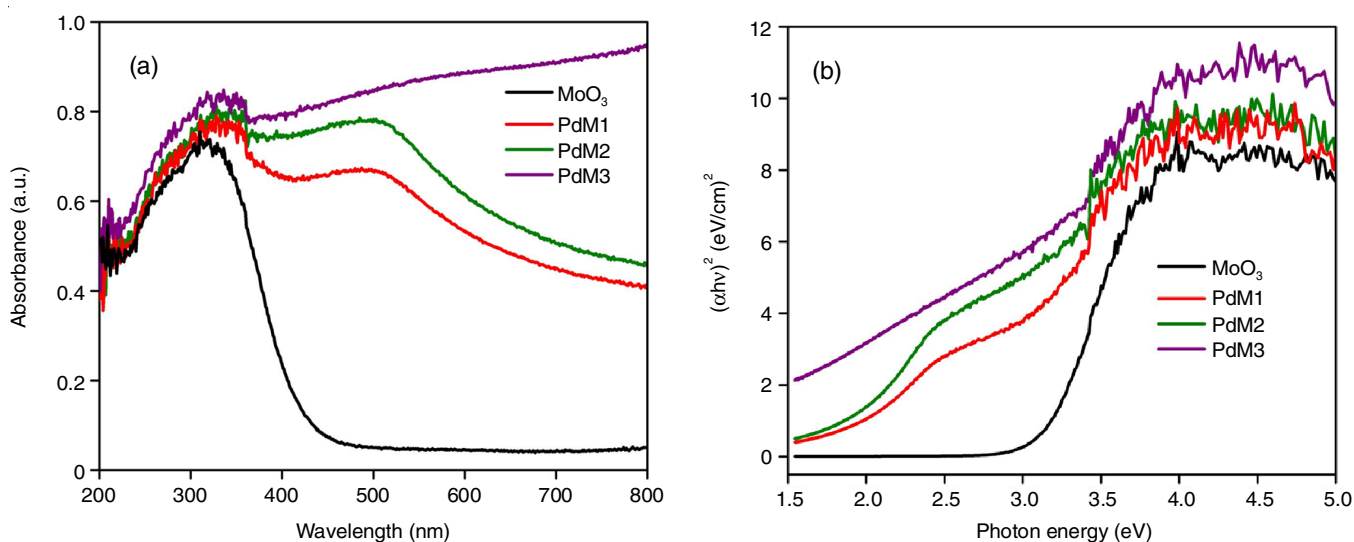
Fig. 6. (a) The UV light absorbance spectrum (in term of Kubelka-Munk equivalent absorbance units) of the pure α-MoO₃ (a) and Pd loaded α-MoO₃ (b) (αhν)² *vs.* hν plots of pure α-MoO₃ (a) and Pd loaded α-MoO₃ nanocomposites

where α is the absorption coefficient of the semiconductor materials, λ is the wavelength materials, h is Planck's constant, ν is the transition light frequency, A is constant quantity which is related to the effective masses associated with conduction band and valence band, E_g is band gap energy. The plots of $(\alpha h\nu)^2$ *versus* hν of the samples are presented in Fig. 6b. The band gap energy values decreased with increase in doping of metallic Pd content in the MoO₃. The band gap energy values were calculated based on their absorption wavelength region and were found to be 3.01 eV for pure α-MoO₃ and 1.81, 1.73 and 0.98 eV for 1, 2 and 3% Pd doped MoO₃ nanocomposites, respectively.

Photoluminescence: To understand the separation and recombination of photogenerated charge carriers of MoO₃, Pd doped MoO₃ nanocomposite, the photoluminescence analysis were examined, which is illuminated in Fig. 7. Photoluminescence (PL) study mainly used to determine the recombination probability and charge separation behaviours of as-synthesized nanocomposites [27]. It is obvious that three main emission
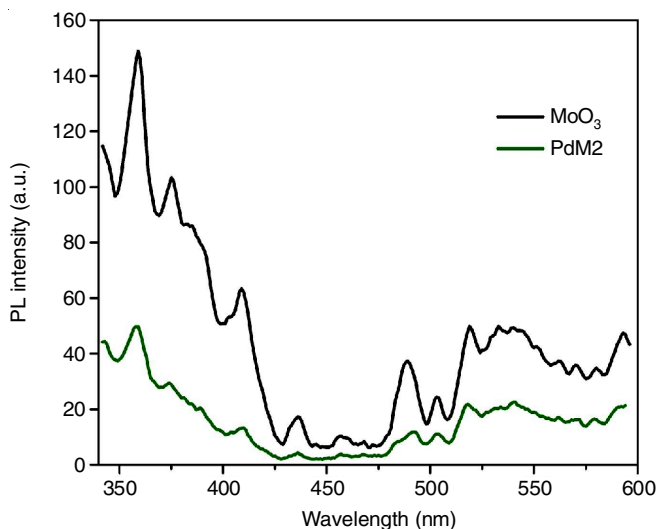
peaks were observed in PL spectra located at 359, 408 and 489 nm. The 2% Pd doped MoO₃ nanocomposite showed the same emission peaks with dramatic decrease in emission yield as compared to pristine MoO₃ [28]. The low PL emission intensity of Pd doped MoO₃ clearly demonstrated that the lowest charge carriers recombination rate and promote the transfer of charges. Additionally, Pd doped MoO₃ nanocomposite have the longer life time of charge carriers and might form greater amount of reactive oxidative species during the photocatalytic reactions.

Photocatalytic activity: The photocatalytic performance of the as-synthesized pure MoO₃, Pd doped MoO₃ nanocomposites were studied towards the degradation of Congo red (model pollutant) dye under visible light illumination as displayed in Fig. 8. The degradation of Congo red dye pollutant was continuously monitored by the absorbance intensity change at main absorption peak at $\lambda = 498$ nm. The peak intensity has been decreased and almost disappears within 70 min of irradiations. It is obviously that the photocatalytic activity of 2% Pd doped MoO₃ nanocomposite showed best efficiency, where 96% of Congo red was degraded within 60 min. The enhancement can be mainly ascribed to Pd nanoparticles has been perfectly anchored on the active sites of MoO₃ nanorods that supress the electron-hole recombinations. When the doping percentage of Pd is over 2%, the photocatalytic activity was decreased due to the excesses of Pd act as recombination centers for electrons and holes [29]. Based on the results, 2% Pd doped MoO₃ catalyst exhibited the superior activity for degradation of Congo red among these as prepared Pd doped MoO₃ nanocomposites and pure MoO₃. No photodegradation occurred in Congo red solution without photocatalyst and with catalyst in the dark condition (Fig. 8b). The reaction of Congo red dye degradation is all fitted to first order kinetics and thus the rate constant can be calculated [30] by the following equation:

$$C = C_0 \exp(-k_{abs}t) \qquad (3)$$

where k_{abs} is the reaction rate constant, C_o is the initial Congo red concentration and C is the Congo red concentration after the time t (min). The rate constant k value for pure MoO₃, 1, 2

Fig. 7. PL spectra of α-MoO₃ and (2%) Pd loaded α-MoO₃ nanocomposite
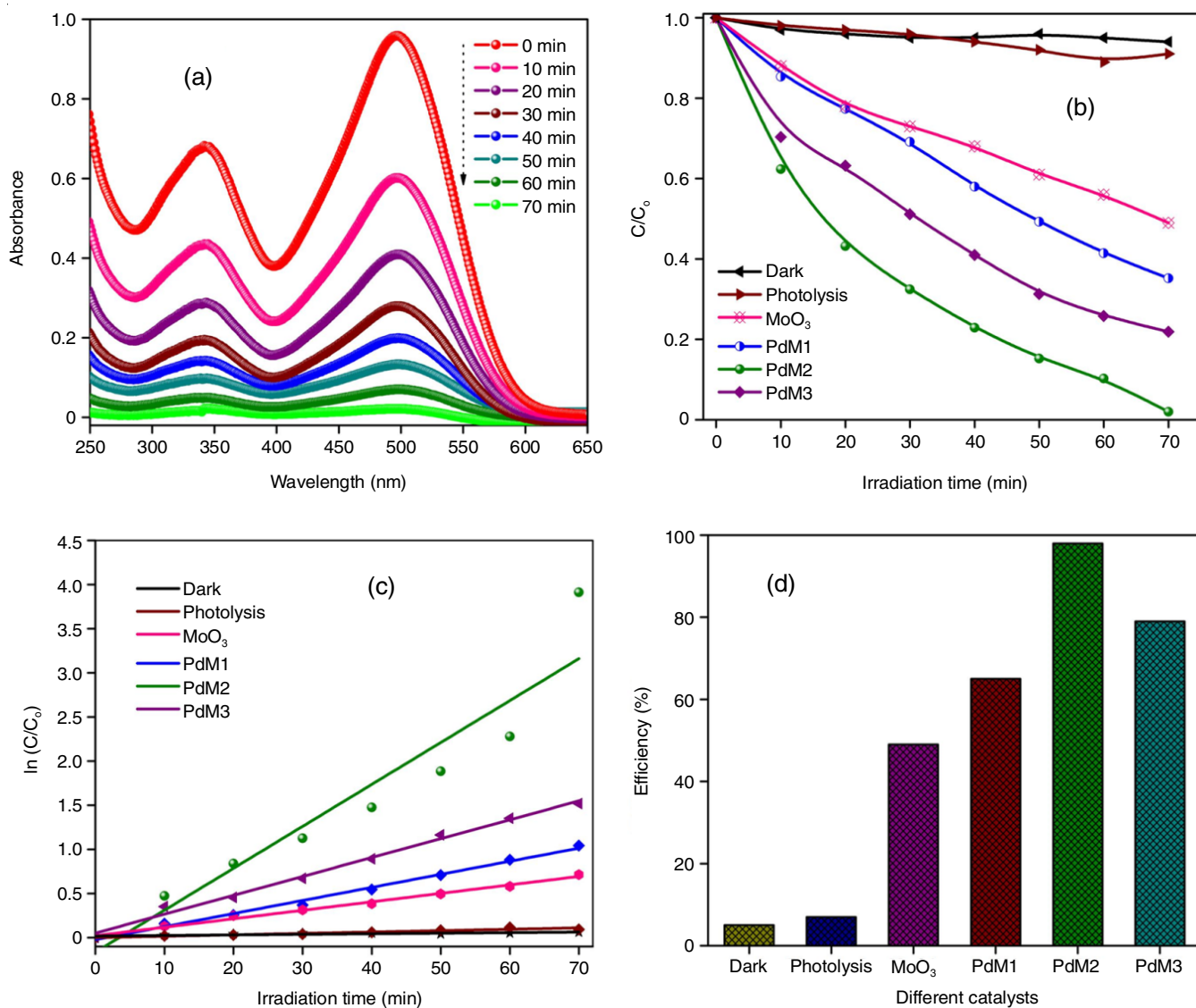
Fig. 8. Congo red organic dye degradation plot (a) UV-vis absorption of Congo red dye (b) concentration *vs* irradiation time plot, (c) reaction kinetic plot, (d) efficiency of dye degradation

and 3% of Pd doped MoO₃ nanocomposites for the degradation of Congo red dye solution were found to be 0.010, 0.015, 0.055 and 0.022 min⁻¹, respectively. The obtained Congo red dye degradation rate constant also indicated that 2% Pd doped MoO₃ nanocomposite showed largest apparent rate constant which is about 5.5 times higher than pure MoO₃ as clearly displayed in Fig. 8c-d.

Mechanism: To understand the mechanism on the enhanced photocatalytic reaction process, a reactive oxidative species experiments have been conducted and the corresponding results are shown in Fig. 9. Three main reagents, including benzoquinone (BQ) for superoxide radical ($O_2^{•-}$), isopropanol (IPA) for hydroxyl radical ($^{•}OH$), ammonium oxalate (AO) for hole (h^+), were employed and their effects on the degradation rate of Congo red dye solution was investigated [31,32]. The photodegradation efficiency was decrease dramatically, when IPA scavenger was added into the photocatalytic reaction process. While the introduction of BQ as a scavenger, a remarkable decrease was observed. Moreover, the addition of AO has made
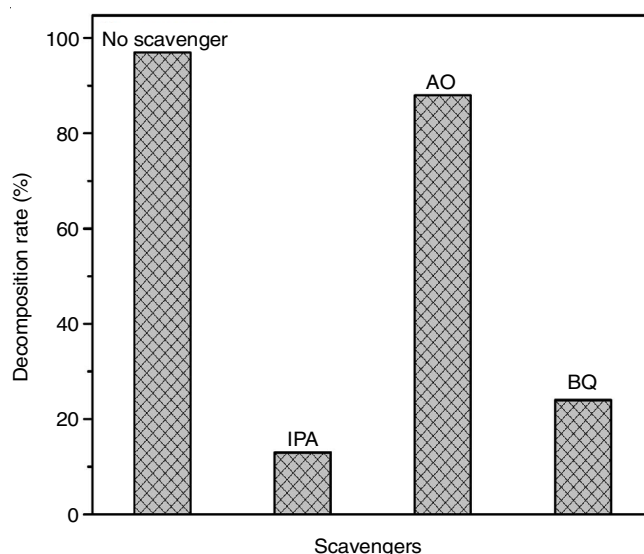
Fig. 9. Effect of different scavengers on the photodegradation of Congo red organic dye solution

TABLE-1 COMPARATIVE DEGRADATION PERCENTAGE OF CONGO RED DYE BY DIFFERENT PHOTOCATALYSTS			
Photocatalyst	Catalyst preparation method	Degradation (%)	Ref.
Cu/SiO_2	Thermochemical method	90	[35]
Fe_2O_3	Combustion	92	[36]
ZnO NPs using *C. edulis*	Microwave assist	97	[37]
CeO_2/Nylon NCTF	Solution cast method	88	[38]
$Ba/Alg/CMC/TiO_2$	Dissipative convective method	91	[39]
$Pd@MoO_3$	Thermochemical method	96	Present work

a very small contribution to the Congo red removal. According to these observations, $O_2^{\bullet-}$ and $^{\bullet}OH$ were the predominant active species for the degradation of Congo red under visible light irradiation.

$$Pd@MoO_3 + h\nu \longrightarrow Pd@MoO_3^* \text{ (Photo excited } e^- + h^+) \quad (4)$$

$$H_2O\ (H^+ + OH^-) + h^+ \longrightarrow H^+ + OH^- \quad (5)$$

$$O_2 + e^- \longrightarrow O_2^- \quad (6)$$

$$CR + OH^- + O_2^- \longrightarrow \text{Intermediate compounds} \quad (7)$$

$$\text{Intermediate compounds} \longrightarrow CO_2 + H_2O + NH_4^+ \quad (8)$$

To obtain better understanding of Pd doped MoO_3 nanocomposite and their enhanced photocatalytic mechanism, the conduction band (CB) and valence band (VB) band edge potential were calculated [33] using the following empirical equations:

$$E_{VB} = \chi - E_0 + \tfrac{1}{2}E_g \quad (9)$$

$$E_{CB} = E_{VB} - E_g \quad (10)$$

where χ is the absolute electronegativity of semiconductor nanomaterials, E_{CB} is the conduction band potential, E_{VB} is the valance band potential, E_o is the standard electrode potential on the hydrogen scale ($= 4.5$ eV *vs.* NHE) and E_g is the optical bandgap energy between CB and VB of the semiconductor [34]. The CB and VB positions of MoO_3 were estimated to 0.355 and 2.655 eV, respectively.

Table-1 shows the comparative degradation percentage of Congo red dye by different photocatalysts as reported in the literature. Thus, present photocatalyst $Pd@MoO_3$ is also matched with other photocatalyst.

Stability and reusability: The stability of the photocatalyst is a crucial parameter for the photocatalytic degradation process [40]. To examine the reusability and stability, recycling experiments were carried out for 2% Pd doped MoO_3 catalyst (Fig. 10). For each new cycle, the photocatalyst was reused for the decolorization of organic dye solution under same conditions. The photocatalysts were collected and washed several time with deionized water/ethanol and dried before reused. The results indicates that after the 5th cycle, degradation efficiency little bit decreased to 88% under visible light irradiation, which probably ascribed to the adsorption of ions/intermediates on the surface of photocatalyst. Hence, the as-prepared Pd doped MoO_3 nanocomposites has higher stability and can be used for visible light active catalyst for environmental sustainability process.

Conclusion

In summary, a series of Pd anchored 1D-MoO_3 nanocomposites is synthesized *via* hydrothermal process. The structure
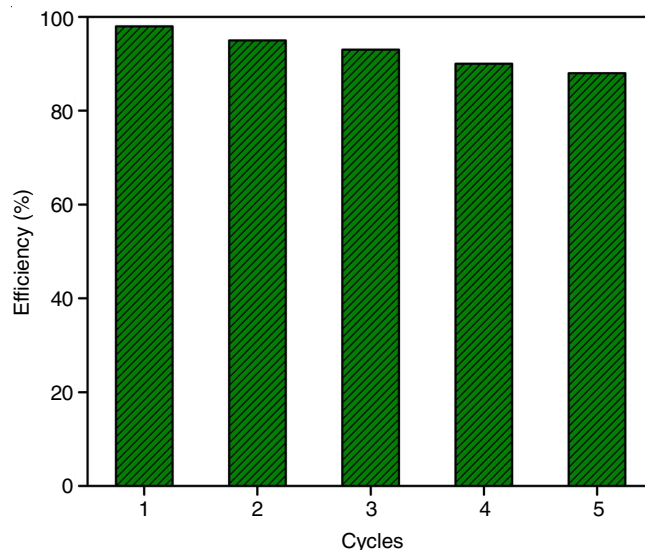
Fig. 10. Recycle process of (2%) Pd loaded α-MoO_3 nanocomposite

and morphology of pure MoO_3 and Pd doped MoO_3 nanocomposites were confirmed by various characterization techniques. Compared to neat MoO_3 nanorods, as-prepared Pd doped MoO_3 nanocomposites show enhanced visible light absorption ability and better charge carriers separation capacity as indicated by UV-DRS and PL analysis. In particular, 2% Pd doped MoO_3 catalyst showed significant enhancement in photocatalytic activity nearly 96% of Congo red dye degradation within 70 min. The much enhanced photocatalytic efficiency may be attributed to the photogenerated electron-hole pairs separation arising from the synergetic bonding of Pd and MoO_3. Moreover, 2% Pd doped MoO_3 photocatalyst exhibited higher cyclic stability even after 5 consecutive cycles. This work provides a new sight for the construction of effective photocatalyst based on MoO_3 nanomaterials for environmental remediation like water purifications and related applications.

CONFLICT OF INTEREST

The authors declare that there is no conflict of interests regarding the publication of this article.

REFERENCES

1. H. Kusic, N. Koprivanac and A.L. Bozic, *J. Photochem. Photobiol. Chem.*, **252**, 131 (2013); https://doi.org/10.1016/j.jphotochem.2012.11.018
2. L. Pereira and M. Alves, eds.: A. Malik and E. Grohmann, Environmental Protection Strategies for Sustainable Development, Springer: New York, vol. 14, pp. 111-162 (2012).
3. S.S. Boxi and S. Paria, *RSC Adv.*, **5**, 37657 (2015); https://doi.org/10.1039/C5RA03421C

4. S.K. Kansal, S. Sood, A. Umar and S.K. Mehta, *J. Alloys Compd.*, **581**, 392 (2013);
https://doi.org/10.1016/j.jallcom.2013.07.069

5. M.M. Kumari and D. Philip, *Spectrochim. Acta A Mol. Biomol. Spectrosc.*, **135**, 632 (2015);
https://doi.org/10.1016/j.saa.2014.07.037

6. K. Saravanakumar and V. Muthuraj, *Optik*, **131**, 754 (2017);
https://doi.org/10.1016/j.ijleo.2016.11.127

7. S.W. Won, S.B. Choi, B.W. Chung, D. Park, J.M. Park and Y.S. Yun, *Ind. Eng. Chem. Res.*, **43**, 7865 (2004);
https://doi.org/10.1021/ie049559o

8. S. Chatterjee, S. Chatterjee, B.P. Chatterjee, A.R. Das and A.K. Guha, *J. Colloid Interface Sci.*, **288**, 30 (2005);
https://doi.org/10.1016/j.jcis.2005.02.055

9. K. Saravanakumar, P.S. Kumar, J.V. Kumar, S. Karuthapandian, R. Philip and V. Muthuraj, *Energy Environ. Focus*, **5**, 50 (2016);
https://doi.org/10.1166/eef.2016.1192

10. Y. Ma, Y. Jia, Z. Jiao, L. Wang, M. Yang, Y. Bi and Y. Qi, *Mater. Lett.*, **157**, 53 (2015);
https://doi.org/10.1016/j.matlet.2015.05.095

11. L. Huang, H. Xu, R. Zhang, X. Cheng, J. Xia, Y. Xu and H. Li, *Appl. Surf. Sci.*, **283**, 25 (2013);
https://doi.org/10.1016/j.apsusc.2013.05.106

12. B. Kannan, R. Pandeeswari and B.G. Jeyaprakash, *Ceram. Int.*, **40**, 5817 (2014);
https://doi.org/10.1016/j.ceramint.2013.11.022

13. Z. Wang, S. Madhavi and X.W. Lou, *J. Phys. Chem. C*, **116**, 12508 (2012);
https://doi.org/10.1021/jp304216z

14. L. Mai, B. Hu, W. Chen, Y. Qi, C. Lao, R. Yang, Y. Dai and Z.L. Wang, *Adv. Mater.*, **19**, 3712 (2007);
https://doi.org/10.1002/adma.200700883

15. T. Liu, B. Li, Y. Hao and Z. Yao, *Chem. Eng. J.*, **244**, 382 (2014);
https://doi.org/10.1016/j.cej.2014.01.070

16. S.L. Prabavathi, P.S. Kumar, K. Saravanakumar, V. Muthuraj and S. Karuthapandian, *J. Photochem. Photobiol. Chem.*, **356**, 642 (2018);
https://doi.org/10.1016/j.jphotochem.2018.02.007

17. X. Cao, B. Zheng, W. Shi, J. Yang, Z. Fan, Z. Luo, X. Rui, B. Chen, Q. Yan and H. Zhang, *Adv. Mater.*, **27**, 4695 (2015);
https://doi.org/10.1002/adma.201501310

18. W. Hou and S.B. Cronin, *Adv. Funct. Mater.*, **23**, 1612 (2013);
https://doi.org/10.1002/adfm.201202148

19. Y.F. Zhang and S.J. Park, *J. Catal.*, **355**, 1 (2017);
https://doi.org/10.1016/j.jcat.2017.08.007

20. Y. Zhang, M. Park, H. Kim, B. Ding and S.J. Park, *Appl. Surf. Sci.*, **384**, 192 (2016);
https://doi.org/10.1016/j.apsusc.2016.05.039

21. H. Pang, Y. Wu, X. Wang, B. Hu and X. Wang, *Chem. Asian J.*, **14**, 2542 (2019);
https://doi.org/10.1002/asia.201900493

22. K. Saravanakumar, S. Muthupoongodi and V. Muthuraj, *J. Rare Earths*, **37**, 853 (2019);
https://doi.org/10.1016/j.jre.2018.12.009

23. S. Saravanamoorthy, A.C. Bose and S. Velmathi, *RSC Adv.*, **5**, 99074 (2015);
https://doi.org/10.1039/C5RA17733B

24. A. Chithambararaj, N.S. Sanjini, A.C. Bose and S. Velmathi, *Catal. Sci. Technol.*, **3**, 1405 (2013);
https://doi.org/10.1039/c3cy20764a

25. P. Zhang, T. Song, T. Wang and H. Zeng, *J. Mater. Chem. A Mater. Energy Sustain.*, **5**, 22772 (2017);
https://doi.org/10.1039/C7TA06625B

26. Y.F. Zhang and S.J. Park, *J. Catal.*, **361**, 238 (2018);
https://doi.org/10.1016/j.jcat.2018.03.010

27. K. Saravanakumar, R. Karthik, S.-M. Chen, J. Vinoth Kumar, K. Prakash and V. Muthuraj, *J. Colloid Interface Sci.*, **504**, 514 (2017);
https://doi.org/10.1016/j.jcis.2017.06.003

28. N. Illyaskutty, S. Sreedhar, G. Sanal Kumar, H. Kohler, M. Schwotzer, C. Natzeck and V.P.M. Pillai, *Nanoscale*, **6**, 13882 (2014);
https://doi.org/10.1039/C4NR04529G

29. K. Saravanakumar, V. Muthuraj and S. Vadivel, *RSC Adv.*, **6**, 61357 (2016);
https://doi.org/10.1039/C6RA10444D

30. S. Lakshmi Prabavathi and K. Saravanakumar, *Colloids Surf. A Physicochem. Eng. Asp.*, **581**, 123845 (2019);
https://doi.org/10.1016/j.colsurfa.2019.123845

31. K. Saravanakumar, M.M. Ramjan, P. Suresh and V. Muthuraj, *J. Alloys Compd.*, **664**, 149 (2016);
https://doi.org/10.1016/j.jallcom.2015.12.245

32. M. Dhanalakshmi, K. Saravanakumar, S. Lakshmi Prabavathi, M. Abinaya and V. Muthuraj, *J. Alloys Compd.*, **763**, 512 (2018);
https://doi.org/10.1016/j.jallcom.2018.05.340

33. M. Mousavi, A. Habibi-Yangjeh and M. Abitorabi, *J. Colloid Interface Sci.*, **480**, 218 (2016);
https://doi.org/10.1016/j.jcis.2016.07.021

34. H. Salari, *J. Photochem. Photobiol. Chem.*, **385**, 112069 (2019);
https://doi.org/10.1016/j.jphotochem.2019.112069

35. T. Tapalad, A. Neramittagapong, S. Neramittagapong and M. Boonmee, *Chiang Mai J. Sci.*, **35**, 63 (2008).

36. S. Dafare, P.S. Deshpande and R.S. Bhavsar, *Indian J. Chem. Technol.*, **20**, 406 (2013).

37. J. Fowsiya, G. Madhumitha, N.A. Al-Dhabi and M.V. Arasu, *J. Photochem. Photobiol. B*, **162**, 395 (2016);
https://doi.org/10.1016/j.jphotobiol.2016.07.011

38. P. Latha, R. Dhanabackialakshmi, P.S. Kumar and S. Karuthapandian, *Sep. Purif. Technol.*, **168**, 124 (2016);
https://doi.org/10.1016/j.seppur.2016.05.038

39. M. Thomas, G.A. Naikoo, M.U.D. Sheikh, M. Bano and F. Khan, *J. Photochem. Photobiol. Chem.*, **327**, 33 (2016);
https://doi.org/10.1016/j.jphotochem.2016.05.005

40. P.S. Kumar, M. Selvakumar, S.G. Babu, S.K. Jaganathan, S. Karuthapandian and S. Chattopadhyay, *RSC Adv.*, **5**, 57493 (2015);
https://doi.org/10.1039/C5RA08783J